Large Differences in Diffuse Solar Radiation among Current-Generation Reanalysis and Satellite-Derived Products

T. CHAKRABORTY[a] AND X. LEE[a]

[a] *School of the Environment, Yale University, New Haven, Connecticut*

(Manuscript received 18 December 2020, in final form 12 May 2021)

ABSTRACT: Although the partitioning of shortwave radiation $K_{\downarrow}$ at the surface into its diffuse ($K_{\downarrow,d}$) and direct beam ($K_{\downarrow,b}$) components is relevant for, among other things, the terrestrial energy and carbon budgets, there is a dearth of large-scale comparisons of this partitioning across reanalysis and satellite-derived products. Here we evaluate $K_{\downarrow}$, $K_{\downarrow,d}$, and $K_{\downarrow,b}$, as well as the diffuse fraction k_d of solar radiation in four current-generation reanalysis datasets (NOAA–CIRES–DOE, NCEP–NCAR, MERRA-2, and ERA5) and one satellite-derived product (CERES) using ≈1400 site-years of observations. Although the systematic positive biases in $K_{\downarrow}$ are consistent with previous studies, the biases in gridded $K_{\downarrow,d}$ and $K_{\downarrow,b}$ vary in direction and magnitude, both annually and across seasons. The intermodel variability in cloud cover strongly explains the biases in both $K_{\downarrow,d}$ and $K_{\downarrow,b}$. Over Europe and China, the long-term (10 yr and longer) trends in $K_{\downarrow,d}$ in the gridded products differ noticeably from corresponding observations and the grid-averaged 35-yr trends show an order of magnitude variability. In the MERRA-2 reanalysis, which includes both clouds and assimilated aerosols, the reductions in both clouds and aerosols reinforce each other to establish brightening trends over Europe, whereas the effect of increasing aerosols overwhelms the effect of decreasing cloud cover over China. The intermodel variability in k_d seen here (from 0.27 to 0.50 from CERES to MERRA-2) suggests substantial differences in shortwave parameterization schemes and their inputs in climate models and can contribute to intermodel variability in coupled simulations. From these results, we call for systematic evaluations of $K_{\downarrow,d}$ and $K_{\downarrow,b}$ in CMIP6 models.

SIGNIFICANCE STATEMENT: The direction of sunlight can be changed by particles and clouds in the air. This is known as diffuse light, and it affects solar energy generation and plant growth. Here, we address a gap in previous studies and compare the diffuse light in global datasets. We find large differences between datasets, explained mostly by differing cloud amounts. When compared with measurements from the ground, we find that these differences exist for most sites and across seasons. The change in diffuse light over the last 35 years also varies widely among datasets. Our results call for larger-scale comparisons of diffuse light in all current-generation global models. Doing so can help us to better constrain future climate change.

KEYWORDS: Clouds; Aerosols; Radiation budgets; Shortwave radiation; Satellite observations; Climate models; Reanalysis data

1. Introduction

Solar radiation is a key driver of Earth's climate system. During its transmission through the atmosphere, it is scattered and absorbed by aerosols, clouds, and gases. Solar radiation incident on the surface ($K_{\downarrow}$) consists of beam radiation ($K_{\downarrow,b}$) and diffuse radiation ($K_{\downarrow,d}$). The former follows the original path of the sunlight, and the latter is the scattered component that deviates from that path. These components are not routinely measured at weather stations (Stephens et al. 2012). Instead, climatic and ecological studies and solar energy applications generally rely on gridded estimates from atmospheric models, including reanalysis products and global climate models (GCMs). Owing to computational limitations, these models are run at relatively coarse resolutions (from 50 to over 200 km). This leads to simplified versions of radiative transfer codes being implemented in these models, as well as differences in input parameters like clouds and aerosols to those codes, both of which influence the estimated radiation fields (Oreopoulos et al. 2012). Systematic biases exist in these model estimates. It is well known that $K_{\downarrow}$ is overestimated by most atmospheric models due in large part to the underestimation of cloud cover (Markovic et al. 2009; Bosilovich et al. 2011; Kennedy et al. 2011; Zhao et al. 2013; Wild et al. 2015; Zhang et al. 2016). This overestimation will lead to surface warming (Chakraborty and Lee 2019) and also increase the energy returned to the atmosphere through heat and moisture fluxes, which may artificially strengthen the hydrological cycle (Wild et al. 1998).

Diffuse radiation $K_{\downarrow,d}$ remains a relatively understudied component of Earth's radiation budget. Several studies have demonstrated enhanced carbon uptake and evaporative fraction at various scales with increasing $K_{\downarrow,d}$ (Knohl and Baldocchi 2008; Mercado et al. 2009; Yue and Unger 2017; Rap et al. 2018; Chakraborty et al. 2021). Thus, a better constraint on $K_{\downarrow,d}$ can improve our ability to predict the surface energy, water, and carbon budgets. Accurate estimates of the direct/diffuse partitioning of $K_{\downarrow}$ are also important for solar energy applications, particularly concentrating solar power (Lee et al. 2016).

Supplemental information related to this paper is available at the Journals Online website: https://doi.org/10.1175/JCLI-D-20-0979.s1.

Corresponding author: T. Chakraborty, tc.chakraborty@yale.edu

DOI: 10.1175/JCLI-D-20-0979.1

© 2021 American Meteorological Society. For information regarding reuse of this content and general copyright information, consult the AMS Copyright Policy (www.ametsoc.org/PUBSReuseLicenses).

This study is concerned with biases in surface $K_{\downarrow,d}$ in retrospective analysis or reanalysis datasets, which assimilate observations of some variables to constrain other modeled variables (Kalnay et al. 1996). These observationally constrained datasets represent our best estimates of the current and historical global climate system. Although site-level comparisons of radiation transfer codes that also consider $K_{\downarrow,d}$ have been performed in the past (Oreopoulos et al. 2012), how accurately reanalysis models simulate $K_{\downarrow,d}$ remains largely unknown at the global scale. To our best knowledge, only a couple of regional-scale evaluations of $K_{\downarrow,d}$ from reanalysis data are available, both for the ERA5 reanalysis (Jiang et al. 2019b, 2020). The second activity of an ongoing intermodel comparative project called Radiative Forcing Intercomparison Project (RFMIP) requests modeling centers to provide broadband fluxes based on their radiative transfer codes, but does not explicitly require the partitioning of $K_{\downarrow}$ into $K_{\downarrow,d}$ and $K_{\downarrow,b}$ (Pincus et al. 2016).

The lessons learned about model biases in $K_{\downarrow}$ are not necessarily applicable to $K_{\downarrow,d}$. The $K_{\downarrow,b}$ incident on the surface is controlled by the total extinction of a light beam as it transmits through the atmosphere, while $K_{\downarrow,d}$ is a function of the scattered sunlight (Liu and Jordan 1960). Thus, one can hypothetically fix the overestimation of $K_{\downarrow}$ in modeled products by increasing aerosols or clouds or through statistical bias-correction algorithms (Zhao et al. 2013), but with unknown individual biases in $K_{\downarrow,d}$ and $K_{\downarrow,b}$. Since aerosols and clouds are parameterized differently in different gridded products, including, but not limited to, prescriptions of cloud droplet size distribution, cloud overlap, and aerosol properties, our hypothesis is that the biases in $K_{\downarrow,d}$ and $K_{\downarrow,b}$ are less systematic in direction than that seen for $K_{\downarrow}$ in previous studies and strongly controlled by the cloud and aerosol inputs (Wild et al. 2015). To test these hypotheses, the specific objectives of this study are the following:

1) to perform a systematic evaluation of the monthly $K_{\downarrow,b}$, $K_{\downarrow}$ and $K_{\downarrow,d}$ in gridded data products, including five current-generation reanalysis datasets (NOAA–CIRES–DOE, NCEP–NCAR, JRA-55, MERRA-2, and ERA5; only $K_{\downarrow}$ for JRA-55) and one satellite-derived product (CERES),
2) to examine the differences in these variables between the gridded data products benchmarked against observations at the annual and seasonal time scales,
3) to evaluate the ability of the gridded products to capture long-term changes in these variables for Europe and China, two regions that have relatively high densities of ground-based observations and have several previous relevant studies to compare the results, and
4) to discuss potential sources of biases and intermodel variability, particularly due to cloud cover and atmospheric aerosols, in these datasets.

2. Methods

a. Global reanalysis products

We used monthly gridded data from five reanalysis products: 1) NOAA–CIRES–DOE—the Twentieth Century Reanalysis, version 3, from the National Oceanic and Atmospheric Administration (NOAA), the Cooperative Institute for Research in Environmental Science (CIRES), and the Department of Energy (DOE), 2) NCEP–NCAR—the 50-year reanalysis from the National Centers for Environmental Prediction (NCEP) and the National Center for Atmospheric Research (NCAR), 3) JRA-55—the Japanese 55-year reanalysis, 4) MERRA-2—the Modern-Era Retrospective Analysis for Research and Applications, version 2, and 5) ERA5—the fifth-generation reanalysis from the European Centre for Medium-Range Weather Forecasts (ECMWF). These represent the latest iteration of the major global reanalyses for research and applications. Note that although the Climate Forecast System Reanalysis (CFSR; Saha et al. 2010) is newer than the NCEP–NCAR reanalysis, it does not publicly archive $K_{\downarrow,d}$. Table 1 summarizes important information about the products considered in the study. Short descriptions of the datasets are given below.

1) NOAA–CIRES–DOE

This reanalysis assimilates surface pressure observations to provide estimates of the historical climate state (Slivinski et al. 2019). In addition to improvements in the assimilation system, the latest version of the reanalysis includes a higher-resolution forecast model, more assimilated pressure observations, and better representation of storm intensity. The radiative transfer model for shortwave in this reanalysis interacts with fractional cloud cover, modeled O_3, time-varying CO_2, volcanic aerosols, and solar variations (Hou et al. 2002).

2) NCEP–NCAR

This reanalysis assimilates data from a wide variety of weather observation including pressure measurements over land, pressure, temperature, and specific humidity measurements over oceans, radiosonde profiles, temperature and wind data observed from aircraft, and satellite-derived cloud-tracked wind data (Kistler et al. 2001). The shortwave parameterization in this reanalysis is based on the work by Lacis and Hansen (1974).

3) JRA-55

The JRA-55 reanalysis improves upon the previous JRA-25 product with an updated assimilation system, more ingested observations, a newer longwave radiation scheme, and higher-resolution forecasts (Kobayashi et al. 2015). The shortwave radiation is parameterized considering random overlap of clouds, H_2O absorption based on Briegleb (1992), O_2, O_3, and CO_2 absorption based on Freidenreich and Ramaswamy (1999), and assuming standard atmospheric aerosol profiles with optical depths adjusted using monthly aerosol climatology. It only archives gridded data for $K_{\downarrow}$.

4) MERRA-2

The MERRA-2 reanalysis is a recent global reanalysis product that assimilates bias-corrected satellite observations of aerosols and clear-sky irradiances (Randles et al. 2017). It also uses observed precipitation to force the land surface model. The shortwave radiation scheme is based on Chou and Suarez (1999) and the latest version of the Goddard Earth Observing System (GEOS-5) assimilates newer satellite observations.

TABLE 1. Summary of the global gridded products considered in this study. The global means and interannual standard deviations of the variables of interest for Common Period I (2001–15) are also noted.

Data product	Spatial resolution	Temporal coverage	Reference	Global $K_{\downarrow}$ ($W\,m^{-2}$)	Global $K_{\downarrow,d}$ ($W\,m^{-2}$)	Global $K_{\downarrow,b}$ ($W\,m^{-2}$)	Global k_d (—)
NOAA–CIRES–DOE	1° × 1°	1836–2015	Slivinski et al. (2019)	192.9 ± 0.4	92.2 ± 0.2	100.7 ± 0.5	0.478 ± 0.002
NCEP–NCAR	1.85° × 1.85°	1948–present	Kistler et al. (2001)	205.3 ± 0.6	81 ± 0.3	124.3 ± 0.6	0.394 ± 0.002
JRA-55	0.562° × 0.562°	1958–present	Kobayashi et al. (2015)	189 ± 0.8	—	—	—
MERRA-2	0.5° × 0.625°	1980–present	Randles et al. (2017)	185.6 ± 0.7	52.8 ± 0.4	132.8 ± 1	0.284 ± 0.003
ERA5	0.25° × 0.25°	1979–present	Hersbach et al. (2020)	187.9 ± 0.4	63.7 ± 0.1	124.2 ± 0.4	0.339 ± 0.001
CERES	1° × 1°	2000–19	Rutan et al. (2015)	185.4 ± 0.3	102.6 ± 0.7	82.8 ± 0	0.553 ± 0.004

The total aerosol optical depth (AOD) in MERRA-2 has been evaluated against independent observations (Buchard et al. 2017).

5) ERA5

The ERA5 reanalysis uses the recently developed Integrated Forecasting System to improve upon its predecessor (Hersbach et al. 2020). In addition to the finer horizontal model resolution, ERA5 has consistent hourly outputs, improvements in the dynamical core, and a four-dimensional variational data assimilation system (like JRA-55). Standardized sets of long-term forcing for aerosols, greenhouse gases, and O_3 are taken from the World Climate Research Programme (WCRP), and the McRad scheme is used to parameterize radiation (Morcrette et al. 2008).

b. Satellite-derived estimates

In addition to the reanalysis products, we used the satellite-derived monthly gridded $K_{\downarrow}$ and $K_{\downarrow,d}$ data in the latest version of the Clouds and the Earth's Radiant Energy System (CERES) synoptic product, (CERES SYN1deg Ed4.1; Rutan et al. 2015). The dataset is well constrained by observations due to direct measurements of the top of the atmosphere components and the use of aerosol and cloud observations from satellites, including those carrying the Moderate Resolution Imaging Spectroradiometer (MODIS), in the radiative transfer code.

c. Ground-based point observations

The Global Energy Balance Archive (GEBA) is a repository of energy flux measurements at Earth's surface (Gilgen and Ohmura 1999) and is the most comprehensive global database of observed mean monthly surface radiation components currently available. Here, we used the latest iteration of the database (Wild et al. 2017) after removing sites with missing data and applying the following quality control steps:

1) We considered only the observations not flagged as erroneous by the database's quality control procedure (thus, data with flags 5, 6, 7, and 8 were used)
2) Observations for which the monthly means were $0\,W\,m^{-2}$ were not considered since they are primarily due to either instrument errors or during polar nights.
3) We removed observations if the diffuse fraction, $k_d = K_{\downarrow,d}/K_{\downarrow}$, exceeded 1 or was 0.
4) Although there are many more stations with $K_{\downarrow}$ measurements than $K_{\downarrow,d}$ measurements, to keep the number of sites consistent we only considered those with simultaneous observations of $K_{\downarrow}$ and $K_{\downarrow,d}$ in most cases (except for examining long-term trends; see section 2d).

After data screening, we obtained 221 stations (the distribution of stations is shown in Fig. S1 in the online supplemental material) with a total of 16 589 site-months of data between 1980 and 2015. Only a few GEBA sites have direct measurements of $K_{\downarrow,b}$. For evaluating modeled $K_{\downarrow,b}$, the observed $K_{\downarrow,b}$ was computed as the difference between $K_{\downarrow}$ and $K_{\downarrow,d}$.

d. Data processing and metrics for evaluation

We extracted monthly $K_{\downarrow,d}$, $K_{\downarrow,b}$, and $K_{\downarrow}$ from the gridded datasets from the start of 1980 to the end of 2019. Only $K_{\downarrow}$ was extracted for JRA-55 since it does not publicly archive $K_{\downarrow,d}$ or $K_{\downarrow,b}$. For the overall evaluation against GEBA, all the grids overlapping the observational sites and months between 2001 and 2015 were used. This period is common to all the six datasets and is referred to as "Common Period I." For cases where multiple sites were within one grid box, the same grid value was compared with each of those observations. For NCEP–NCAR, dataset with the lowest resolution, roughly 12% of the sites share a common grid with another site, while only 2% of sites share a common grid when using the highest-resolution dataset (ERA5). Four metrics were used to evaluate the modeled data, including the coefficient of determination r^2, root-mean-square error (RMSE), mean bias error (MBE), and mean percentage error (MPE).

To examine intermodel variability at annual and seasonal scales, we chose Common Period I and used the CERES data as reference. To avoid mixing the seasonality of the two hemispheres, we only used sites and grids in the Northern Hemisphere when examining seasonality. Although point-based observations of surface radiation fields are not always comparable to gridded estimates due to how models represent clouds, at the monthly scale, these uncertainties are reduced (see section 4b).

We restricted our trend analysis to Europe and China between 1980 and 2015. This period, here termed "Common Period II," is longer than the CERES data period but covered by all the five reanalysis products (Table 1). These two regions have more sites with continuous data coverage than other regions of the world. We calculated temporal trends for the sites

with at least a total of 10 years of data (not necessarily contiguous years). Site-averaged time trends of the gridded model data were based on the same measurement years and the grids containing these GEBA sites. The threshold of 10 years, although somewhat arbitrary, was used, not to estimate the true 35-yr trend but to examine whether the gridded products showed similar trends during the corresponding time frame. Similar thresholds have been used in other studies that have examined long-term trends in $K_{\downarrow}$ (Yang et al. 2019; Schwarz et al. 2020). Since few of the sites have both observations of $K_{\downarrow,d}$ and $K_{\downarrow}$ that satisfy all the above criteria, we used a different subset of measurements for $K_{\downarrow}$ and $K_{\downarrow,d}$ over these regions. This left us with 28 (7) stations over Europe (China) for examining $K_{\downarrow}$ trends, and 15 (5) sites over Europe (China) for $K_{\downarrow,d}$ trends. Before using these stations, however, we also tested for change/breakpoints in the time series data using the standard normal homogeneity test (Alexandersson 1986). Considering only those stations that show no breakpoints at the 95% significance level, we got 24 (4) stations over Europe (China) for $K_{\downarrow}$ and 8 (4) stations over Europe (China) for $K_{\downarrow,d}$. We also calculated the grid-averaged modeled trend for the entire period (1980–2015) using all the grids that fall within Europe and China. Before finding the grids intersecting these two regions, the five reanalysis products were regridded to $1° \times 1°$ grids, the grid size of CERES, using bilinear interpolation, which is appropriate because of the spatial continuity in these variables at the annual time scale. This regridded data were also used to demonstrate grid-by-grid difference in multiyear average values between the products (see section 3b). In all cases, the trends were based on the annual average value regressed against the year of observation, with the statistical significance of the trends calculated. We also estimated cloud cover, top-of-the-atmosphere $K_{\downarrow}$, and AOD (from MERRA-2) for Europe and China and globally to examine the reasons for some of these biases.

3. Results

a. Overall evaluation and annual intercomparisons

The global mean $K_{\downarrow}$ varies from 185.4 W m^{-2} (CERES) to 205.3 W m^{-2} (NCEP–NCAR) for Common Period I (2001–15), based on all model grids (Table 1). In comparison, Wild et al. (2015) found a multimodel mean $K_{\downarrow}$ of 189.1 W m^{-2} based on 43 CMIP5 models for 2000–04. For the grid-years that coincide with the GEBA observations, the modeled mean $K_{\downarrow}$ varies from 165.2 W m^{-2} (CERES) to 208.1 W m^{-2} (NCEP–NCAR), and the observed mean $K_{\downarrow}$ is 162.5 W m^{-2}. All the reanalysis datasets capture the seasonal (Fig. 3) and geographic distributions of the GEBA-observed $K_{\downarrow}$ relatively well, with the overall r^2 varying from 0.9 for NOAA–CIRES–DOE and NCEP–NCAR to 0.96 for CERES (Table 2). As expected, CERES performs better than all the reanalysis products, both in terms of variability ($r^2 = 0.97$) and bias (MBE = 2.6 W m^{-2}).

The global mean $K_{\downarrow,b}$ varies from 82.8 W m^{-2} (CERES) to 132.8 W m^{-2} (MERRA-2) during Common Period I, based on all model grids. The sign of the error in $K_{\downarrow,b}$ is less consistent across the different products than the error in $K_{\downarrow}$ (Fig. 1). While NCEP–NCAR, MERRA-2, and ERA5 overestimate $K_{\downarrow,b}$ (MBE = 36.8, 39.9, and 17.4 W m^{-2}, respectively), NOAA–CIRES–DOE and CERES underestimate it (MPE = −4.3 and −16.8 W m^{-2}, respectively; Table 2). Among the reanalyses, ERA5 performs the best at capturing the global variability in $K_{\downarrow,b}$ ($r^2 = 0.9$), and NCEP–NCAR performs the worst ($r^2 \approx 0.73$).

The global mean $K_{\downarrow,d}$ varies from 52.8 W m^{-2} (MERRA-2) to 102.6 W m^{-2} (CERES), and diffuse fraction k_d varies from 0.28 (MERRA-2) to 0.55 (CERES) during Common Period I based on all model grids (Table 1). For the grid-years that coincide with the GEBA observations, k_d ranges from 0.28 (MERRA-2) to 0.55 (CERES), and the observed mean k_d for the quality-controlled GEBA dataset is 0.46. NOAA–CIRES–DOE, NCEP–NCAR, and CERES have positive biases in $K_{\downarrow,d}$ (MBE = 13.8, 8.77, and 19.5 W m^{-2}, respectively; Table 2), and MERRA-2 and ERA5 have negative biases (MBE = −21.4 and −9.9 W m^{-2}, respectively; Table 2). Bias errors in k_d depend on errors in $K_{\downarrow,d}$ and $K_{\downarrow}$. For MERRA-2 and ERA5, $K_{\downarrow}$ is positively biased, and $K_{\downarrow,d}$ is negatively biased (Table 2). Consequently, these two reanalyses underestimate k_d, with MERRA-2 performing the worst among the datasets, with an MBE of −0.18 for all sites. NCEP–NCAR underestimates k_d (MBE = −0.07) because it overestimates $K_{\downarrow}$ more (relatively speaking) than it overestimates $K_{\downarrow,d}$ (Table 2). Even though NCEP–NCAR and NOAA–CIRES–DOE show smaller MBE than MERRA-2, they do not capture the observed variability in k_d well ($r^2 = 0.36$–0.41). ERA5 captures the variability in k_d the best ($r^2 = 0.72$), even better than CERES ($r^2 = 0.67$). CERES overestimates k_d (MBE = 0.09) as it underestimates $K_{\downarrow,b}$ and overestimates $K_{\downarrow,d}$.

Figure 1 shows the scatterplots between gridded and observed k_d, $K_{\downarrow,d}$, and $K_{\downarrow,b}$ for all common GEBA site-months, with each data point representing a monthly mean and the color representing the density of data. Figure S2 in the online supplemental material shows the scatterplots for total $K_{\downarrow}$. The scatter is a result of both natural (seasonal and geographic) variations and measurement and model errors. As discussed earlier, the gridded data show larger variability than observations, and the biases in gridded $K_{\downarrow,d}$ and $K_{\downarrow,b}$ across products is less systematic in sign than the consistent overestimation seen for $K_{\downarrow}$ (Fig. S1 and Table 2). This lack of consistency is evident in the scatterplots. For instance, although the line of best fit for the gridded $K_{\downarrow,b}$ data is ERA5 is almost identical to the 1:1 line, the slope is only 0.7 for $K_{\downarrow,d}$ since the intercept. For CERES, the line of best fit is less than the 1:1 line for $K_{\downarrow,b}$, but is greater than 1:1 for $K_{\downarrow,d}$, demonstrating the underestimation of $K_{\downarrow,b}$ and overestimation of $K_{\downarrow,d}$ by this dataset with an intercept close to zero. In general, more scatter is seen for NOAA–CIRES–DOE and NCEP–NCAR data and the least for ERA5 and CERES. For NOAA–CIRES–DOE, the large scatter for k_d suggests that the dataset cannot adequately capture the spatiotemporal distribution of this variable.

b. Site-level evaluation and spatial patterns

Figures 2a and 2b map the MBE in $K_{\downarrow}$ at individual GEBA sites for NCEP–NCAR and CERES, respectively, for Common Period I. Similarly, Figs. 2c and 2d display the site-level MBE

TABLE 2. Evaluations of monthly mean total incoming shortwave radiation $K_{\downarrow}$, direct beam radiation $K_{\downarrow,b}$, diffuse radiation $K_{\downarrow,d}$, and diffuse fraction k_d at the surface against the common GEBA observations for Common Period I (2001–15). Statistical summaries of the evaluations include the intercept and slope of the line of best fit, coefficient of determination r^2, mean bias error, and mean percentage error. The sample size is 14 155 in all cases.

	Slope	Intercept	r^2	RMSE	MBE	MPE	Slope	Intercept	r^2	RMSE	MBE	MPE
			$K_{\downarrow}$						$K_{\downarrow,b}$			
NOAA–CIRES–DOE	1	8.82	0.9	30.16	9.52	5.9	0.89	6.15	0.75	34.66	−4.28	−4.4
NCEP–NCAR	1.01	43.91	0.9	53.45	45.56	28	0.89	47.59	0.73	51.43	36.79	38.2
JRA-55	0.98	18.25	0.93	26.71	15.27	9.4	—	—	—	—	—	—
MERRA-2	1.03	13.06	0.94	28.22	18.54	11.4	1.08	32.11	0.86	49.44	39.9	41.5
ERA5	0.99	9.72	0.96	18.04	7.51	4.6	0.99	18.15	0.9	27.17	17.38	18.1
CERES	0.98	6.45	0.97	15.72	2.65	1.6	0.8	2.7	0.88	28.32	−16.82	−17.5
			$K_{\downarrow,d}$						k_d			
NOAA–CIRES–DOE	0.94	17.68	0.75	21.67	13.8	20.8	0.7	0.21	0.41	0.16	0.08	16.4
NCEP–NCAR	0.73	26.91	0.66	20.01	8.77	13.2	0.41	0.2	0.36	0.14	−0.07	−14.5
MERRA-2	0.61	4.84	0.83	25.84	−21.36	−32.2	0.56	0.03	0.62	0.2	−0.18	−38.4
ERA5	0.7	9.86	0.86	16	−9.87	−14.9	0.72	0.05	0.72	0.11	−0.08	−17.5
CERES	1.28	0.89	0.86	26.61	19.47	29.4	0.76	0.2	0.67	0.13	0.09	19.8

in NCEP–NCAR and CERES for $K_{\downarrow,d}$. Bias maps for the other data products can be found in Fig. S3 in the online supplemental material.

The site-level MBE patterns of $K_{\downarrow}$ and $K_{\downarrow,d}$ are consistent with the overall evaluation in the previous subsection. The reanalysis products show a positive $K_{\downarrow}$ bias for the majority of the GEBA sites (80.5% for NOAA–CIRES–DOE, 98.9% for NCEP–NCAR, 90% for JRA-55, 94.7% for MERRA-2, and 78.9% for ERA5). The NCEP–NCAR reanalysis has the highest $K_{\downarrow}$ MBE among the datasets considered, and ERA5 and CERES have low biases. MERRA-2 underestimates $K_{\downarrow,d}$ for almost all the sites (99.7%; Fig. S1f) and ERA5 underestimates $K_{\downarrow,d}$ for 91.9% of the sites (Fig. S3g). NOAA–CIRES–DOE, NCEP–NCAR, and CERES overestimate $K_{\downarrow,d}$ for 93.6%, 76.5%, and 98% of the sites, respectively (Figs. 3c,d and Fig. S3e).

Since CERES captures both the magnitude and variability of $K_{\downarrow}$ more accurately than the reanalyses (Table 2), here we use CERES as the reference to examine anomaly hot spots of the reanalysis products for Common Period I (Fig. 3c; Fig. S4 in the online supplemental material). All the reanalysis products show qualitatively similar positive biases from CERES over southern China and along the western coast of South America. NOAA–CIRES–DOE shows some of the largest localized anomalies; positive biases of as much as 100 W m^{-2} are evident over eastern China. Overall, the differences are lower over Europe (0.0 ± 1.2 W m^{-2} for ERA5 to 46.6 ± 2.0 W m^{-2} for NCEP–NCAR; mean ± standard deviation) than over China (12.3 ± 1.4 W m^{-2} for NOAA–CIRES–DOE to 65.6 ± 2.1 W m^{-2} for NCEP–NCAR) for all the reanalysis products, a pattern consistent with site-level evaluations using GEBA observations (Fig. 2; Fig. S3 in the online supplemental material). The closer value between CERES and the reanalyses over Europe could be due to stronger constraints on the energy budget due to more quality-assured assimilated meteorological observations over this region. For reference, the number of common GEBA stations over Europe for Common Period I is 93, while there are only 10 over China, with similar sampling biases expected for assimilated variables. Another potential factor is the influence of higher aerosol loading over China, which is not explicitly represented in most of these datasets.

c. Annual cycle

Figure 3 compares the Northern Hemisphere seasonal patterns in $K_{\downarrow,d}$, $K_{\downarrow}$, and k_d among the datasets and the GEBA observations in the Northern Hemisphere, using the site-months common to the datasets and the GEBA observations for Common Period I. The complete Northern Hemisphere mean seasonal patterns are given in Figs. 3b, 3d, and 3f using all the model grids. The GEBA observations are skewed toward middle to high latitudes; thus Figs. 3a and 3b show a stronger $K_{\downarrow}$ and $K_{\downarrow,d}$ seasonality than Figs. 3b and 3d. For instance, the interseasonal range of $K_{\downarrow}$, or the difference between the monthly maximum and monthly minimum $K_{\downarrow}$ for the average year, is 134.4 W m^{-2} in Fig. 3b and 178.8 W m^{-2} in Fig. 3a for CERES. The data products generally capture the observed seasonality, showing much higher $K_{\downarrow}$ and $K_{\downarrow,d}$ values in the summer than in the winter (Figs. 3a and 3c). Among the datasets, the interseasonal range in site-corresponding $K_{\downarrow}$ varies from 178.8 W m^{-2} in CERES and ERA5 (181 W m^{-2} for GEBA) to 207.7 W m^{-2} in NCEP–NCAR according to Fig. 3a.

In general, there is a larger inconsistency in the $K_{\downarrow,d}$ seasonal variations than the $K_{\downarrow}$ seasonal variations among the datasets. Particularly, the CERES data show a more pronounced $K_{\downarrow,d}$ seasonality (interseasonal range = 101 W m^{-2}) than the GEBA observations (interseasonal range = 70 W m^{-2}) and the other data products (average interseasonal range of 61.6 W m^{-2} for the other products; Fig. 3c).

Globally, the observed k_d is higher in winter and lower in the summer (Fig. 3e). The interseasonal range in k_d varies substantially between the products, with CERES showing the lowest range of 0.03 and NOAA–CIRES–DOE showing the highest range of 0.22 (Fig. 3e). In comparison, the interseasonal range in the corresponding GEBA observations is 0.13. The muted seasonality in CERES is evidently driven by the stronger seasonality for $K_{\downarrow,d}$ in this dataset. Combining all the gridded

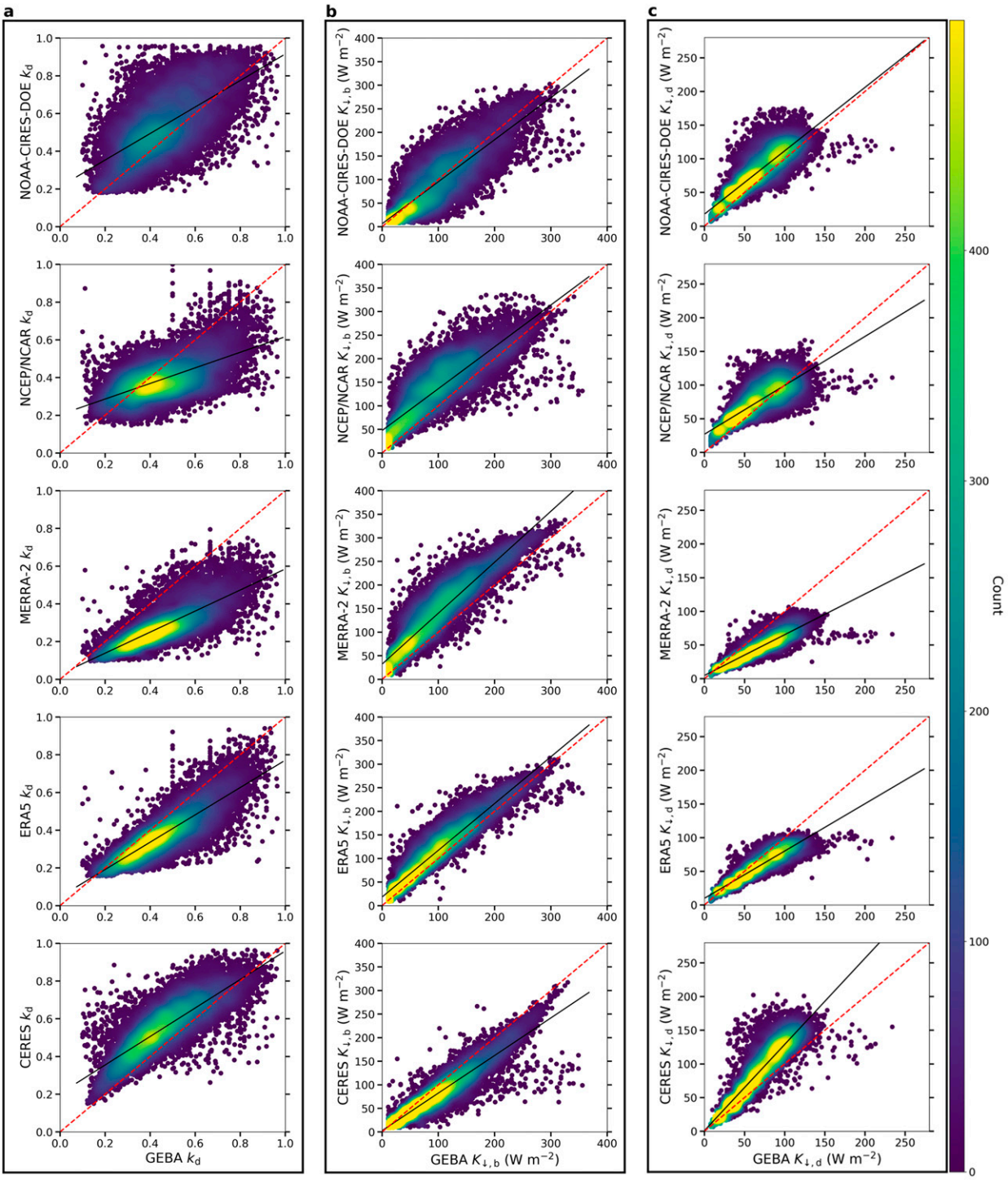

FIG. 1. Evaluations of monthly mean incoming (a) diffuse fraction k_d, (b) beam radiation $K_{\downarrow,b}$, and (c) diffuse radiation $K_{\downarrow,d}$ at the surface of gridded reanalysis and CERES products against the common GEBA observations for Common Period I (2001–15). The red dashed lines represent the 1:1 relationship. Color indicates data density. Statistical summaries of the evaluations are in Table 2.

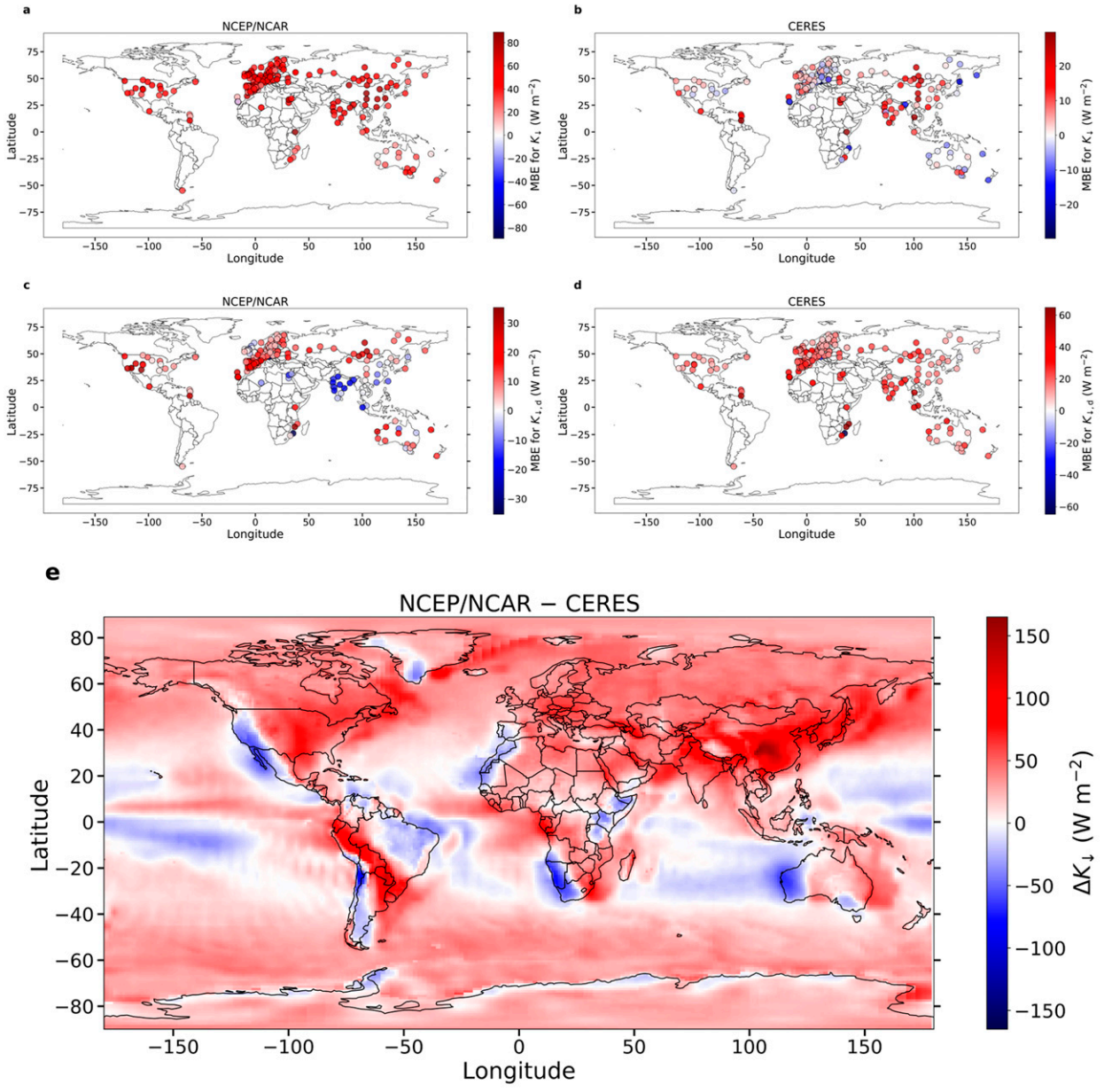

FIG. 2. Site-level MBE in incoming (a),(b) shortwave radiation $K_{\downarrow}$ and (c),(d) diffuse radiation $K_{\downarrow,d}$ at the surface for (left) NCEP–NCAR and (right) CERES data compared with common GEBA observations for Common Period I (2001–15). (e) The gridwise difference in $K_{\downarrow}$ between NCEP–NCAR and CERES data.

products, for the Northern Hemisphere, the spatially averaged interseasonal range in k_d is only 0.05 (Fig. 3f), as compared with 0.13 for the grids corresponding to the GEBA observations, evidently due to the higher frequency of GEBA observations in the higher latitudes.

d. Long-term trends over Europe and China

We analyze the long-term trends in $K_{\downarrow}$ and $K_{\downarrow,d}$ in Europe and China in two ways. First, we calculate the trends using the reanalysis products for Common Period II (1980–2015) and all grid cells in these two regions. The results are presented as solid bars in Fig. 4 with the statistical significance of the trends noted. Over Europe, NOAA–CIRES–DOE shows a slightly negative trend, and the other four reanalysis products show clearly positive trends in $K_{\downarrow}$, with the rate of change varying from $-0.07\,\mathrm{W\,m^{-2}}$ per decade in NOAA–CIRES–DOE to $2.02\,\mathrm{W\,m^{-2}}$ per decade in ERA5 (Fig. 4a). The average trend of the five products is $0.80 \pm 0.74\,\mathrm{W\,m^{-2}}$ per decade (mean ± standard deviation; here standard deviation indicates variation among the five products). The regional mean $K_{\downarrow,d}$ shows an increasing

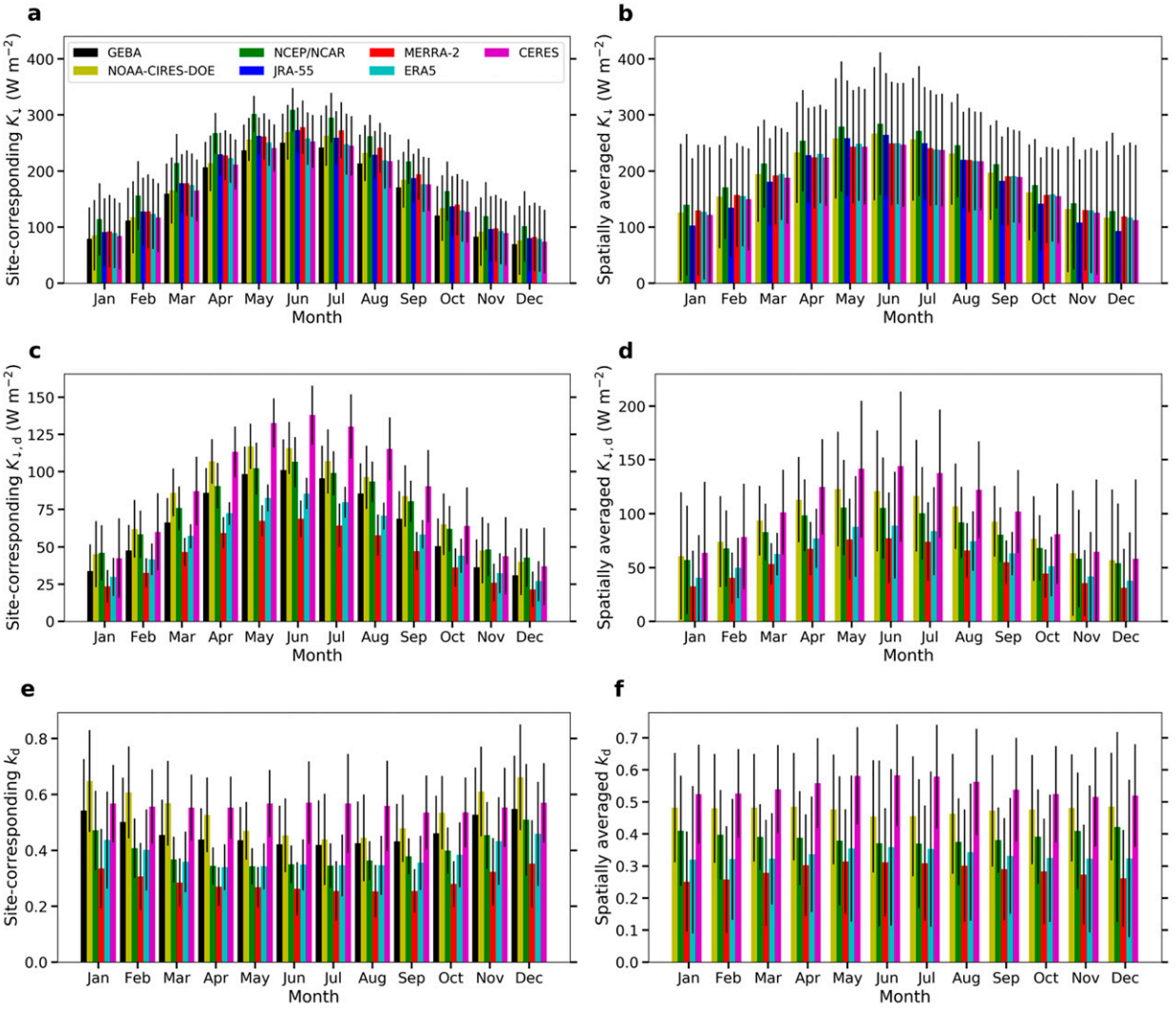

FIG. 3. Seasonal variation in (a) $K_{\downarrow}$, (c) $K_{\downarrow,d}$, and (e) k_d at the surface for all Northern Hemisphere common GEBA sites and the grids overlying the sites for Common Period I (2001–15). (b),(d),(f) The corresponding Northern Hemisphere means from the gridded products for the same period. In all cases, the black lines show the standard deviations [of the site-level data for (a), (c), and (e) and the spatial variability of the grid values for (b), (d), and (f)].

trend according to NCEP–NCAR and decreasing trends according to the other three products (NOAA–CIRES–DOE, MERRA-2, and ERA5), with the rate of change ranging from 0.39 W m^{-2} per decade in NCEP–NCAR to -1.6 W m^{-2} per decade in MERRA-2 (Fig. 4b), with a four-product mean value of -0.86 ± 0.75 W m^{-2} per decade. JRA-55 does not provide $K_{\downarrow,d}$ data.

Over China, the trends in $K_{\downarrow}$ are less consistent than those over Europe. Two products (MERRA-2 and JRA-55) show decreasing trends, and three (NOAA–CIRES–DOE, NCEP–NCAR, and ERA5) show increasing trends. The rate of change varies from -0.73 W m^{-2} per decade (MERRA-2) to 1.76 W m^{-2} per decade (NCEP–NCAR), giving a five-product mean of 0.41 ± 0.88 W m^{-2} per decade. In contrast, all products show decreasing trends in $K_{\downarrow,d}$, giving a four-product mean rate of change of -0.72 ± 0.39 W m^{-2} per decade (Fig. 4d).

Second, we analyze the time trends using the GEBA data and the reanalysis data from the grids containing these GEBA sites and for the same measurement years. Since the number of sites that fulfill all the quality-control criteria, including the homogeneity test, are small (see section 2), we stress that these do not necessarily represent regional trends. Instead, we examine whether the gridded products capture the observed trends for the corresponding periods. The trends for the individual stations included for each region are represented by the circles in Fig. 4, with the overall mean and standard errors for these shown as hatched bars. For 62.5% (15 of 24) of the GEBA sites considered over Europe, we see a positive trend, with an average increasing trend in $K_{\downarrow}$ (2.18 W m^{-2} per

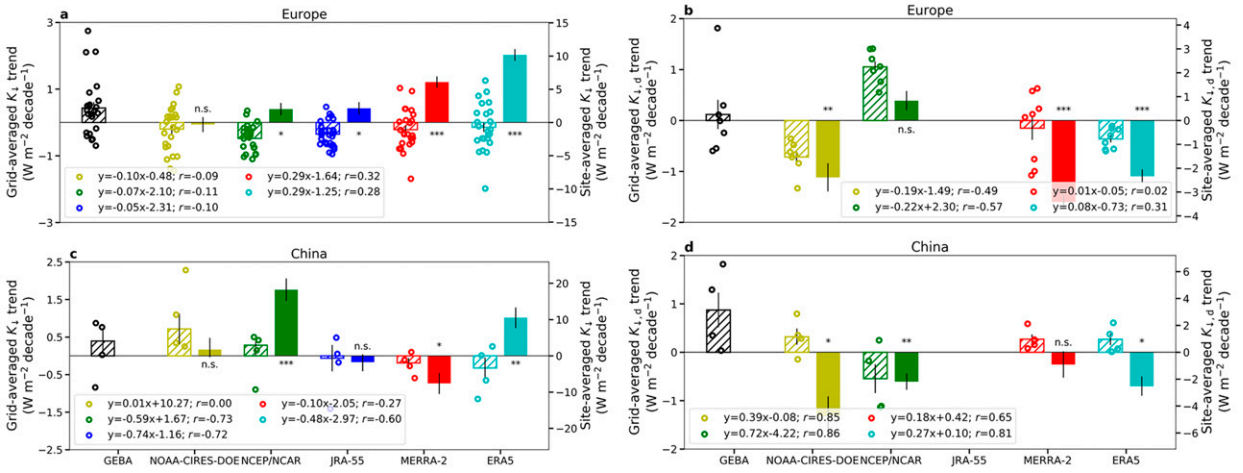

FIG. 4. Long-term trends from gridded and observed data in (left) $K_\downarrow$ and (right) $K_{\downarrow,d}$ at the surface over (a),(b) Europe and (c),(d) China. The long-term trends in the GEBA observations with at least 10 years of data in Common Period II (1980–2015), as well as the corresponding trends for the overlapping grids from the gridded products, are shown with circles. The hatched bars show the mean (± standard error) of the trends based on these circles. Equations of lines representing the associations between the observed and the corresponding modeled trends are in the legends. The solid bars show the grid-area-averaged regional values for the gridded reanalysis products for the entire period (1980–2015), and the error bars represent the standard errors. The p values of the grid-averaged trends are indicated by asterisks, with three asterisks representing $p < 0.0001$, two for $p < 0.001$, and one for $p < 0.05$, with n.s. indicating no significance at the 0.05 level.

decade), which is consistent with existing studies (Wild 2012, 2016; Schwarz et al. 2020). None of the reanalysis products capture the direction of the mean brightening trend for the corresponding grids and years, although the regressions between the observed and modeled trends in $K_\downarrow$ are positive for ERA5 ($r = 0.28$) and MERRA-2 ($r = 0.32$). For $K_{\downarrow,d}$, only one-half of the six GEBA sites show decreasing trends. Among the reanalysis products, only ERA5 captures (weakly) the corresponding trends ($r = 31$).

Over China, three of the four GEBA sites show a brightening trend (Fig. 4c), with none of the corresponding reanalysis products capturing the variability of trends between the sites. On the contrary, for $K_{\downarrow,d}$, all the four considered GEBA sites show an increase over time, with all the reanalysis products other than NCEP–NCAR capturing the positive direction of the mean trend.

Several previous studies have examined the long-term trends in $K_\downarrow$ over Europe and China owing to the larger data coverage and strong temporal trends in these regions (Samukova et al. 2014; Sanchez-Lorenzo et al. 2015; Feng et al. 2018; Schwarz et al. 2020). Although the magnitude of the trends varies across studies depending on quality control of the data and the selection of the observation sites and the time periods of interest, most studies have found strong brightening over Europe and weak to negligible brightening over China since the 1980s. For Europe, Sanchez-Lorenzo et al. (2015) found an increasing trend of 3.2 W m^{-2} per decade for $K_\downarrow$ between 1986 and 2012. Similarly, Pfeifroth et al. (2018) found increasing trends between 1.9 and 2.4 W m^{-2} per decade for 1983–2015. Most recently, Schwarz et al. (2020) found an increase in the $K_\downarrow$ absorbed by the surface at a rate of 1.7 W m^{-2} per decade in Europe for the 31-yr period between 1985 and 2015. For the time periods corresponding to the three studies mentioned above, we calculate the five-product mean brightening trends of 0.63, 0.68, and 0.57 W m^{-2} per decade, respectively. Over China, strong brightening trends (by 10.6 W m^{-2} per decade) have been seen for clear-sky conditions between 2006 and 2018 (Yang et al. 2019). For all-sky conditions, the absorbed $K_\downarrow$ at the surface showed a dimming trend of -0.7 W m^{-2} per decade between 1985 and 2009 and a brightening trend of 1.4 W m^{-2} per decade between 2011 and 2015 (Schwarz et al. 2020). We find a five-product mean increase in $K_\downarrow$ by 0.41 W m^{-2} per decade for Common Period II in China. The observed increase in $K_\downarrow$ for the subset of GEBA sites in China is not captured by the reanalyses over the corresponding sites. The overall regional brightening has also been found to be missing in unconstrained CMIP5 model simulations (Moseid et al. 2020).

Observational constraints on long-term trends in $K_{\downarrow,d}$ are much rarer, partly because of the lack of sufficient ground stations that measure this variable, as well as higher uncertainties in these measurements. For Europe, a couple of studies show decreasing trend in $K_{\downarrow,d}$ since the 1980s (Samukova et al. 2014; Wild et al. 2017). We also find a decreasing four-product mean trend of -0.86 W m^{-2} per decade for Common Period II. For China, there are more studies on long-term trends in $K_{\downarrow,d}$, generally showing a decrease in $K_{\downarrow,d}$ until the 1990s, followed by an increase till 2010 (Wang and Yang 2014). For northern China, $K_{\downarrow,d}$ showed an increasing tendency from 1959 to 2016 according to a recent study (Feng et al. 2018), but a strong decreasing tendency for the Beijing and Shenyang stations, both in the northern China, according to another study (Wang et al. 2020). We find a decreasing four-product

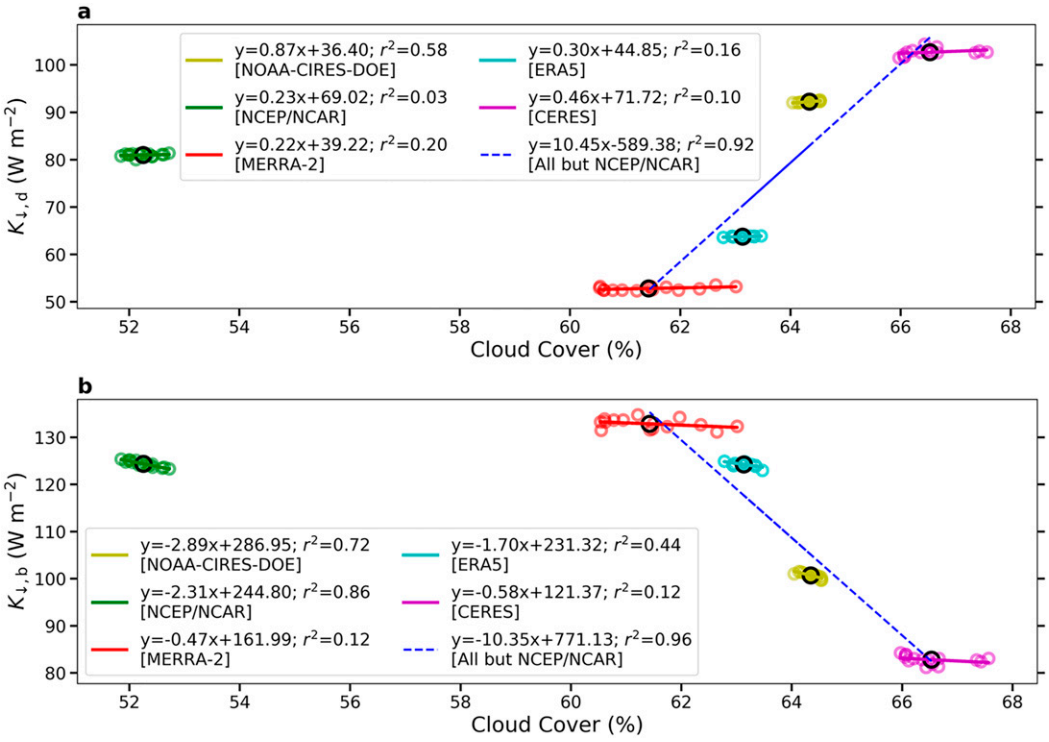

FIG. 5. Associations between percentage cloud cover and (a) $K_{\downarrow,d}$ and (b) $K_{\downarrow,b}$ for Common Period I (2001–15). Each colored circle represents an annual mean value, and the black circle shows the multiyear average for the gridded product. The lines of best fit and their equations are shown both for individual gridded products and across products (not considering NCEP–NCAR).

mean trend in $K_{\downarrow,d}$ of −2.93 (−0.72) W m^{-2} per decade for Common Period II.

e. *Role of clouds and aerosols on intermodel variability in gridded products*

Previous studies show overestimation of $K_{\downarrow}$ in reanalysis datasets due to the underestimation of clouds (Zhao et al. 2013; Wild et al. 2015; Loeb et al. 2019). Here, we separately analyze the correlation of $K_{\downarrow,d}$ and $K_{\downarrow,b}$ with percentage cloud cover at the global scale, both within the gridded products using annual averages and between the products using multiyear averages for Common Period I (Fig. 5). The datasets show similar spatial patterns in cloud cover (Fig. S5 in the online supplemental material), but large differences in global mean values, ranging from 52.3% in NCEP–NCAR to 66.5% in CERES. In general, products with lower cloud cover have higher average $K_{\downarrow,b}$ and lower $K_{\downarrow,d}$, which makes sense mechanistically. The exception to this strong linear relationship ($r^2 = 0.96$ for $K_{\downarrow,b}$ and 0.92 for $K_{\downarrow,d}$; Fig. 5) is NCEP–NCAR, which has the lowest cloud cover, but not the lowest $K_{\downarrow,d}$ or the highest $K_{\downarrow,b}$. Note that NCEP–NCAR does have the highest $K_{\downarrow}$ (Table 1). Thus, the issue is the partitioning of $K_{\downarrow,d}$ in the product. The underestimation of $K_{\downarrow,b}$ and overestimation of $K_{\downarrow,d}$ in CERES may be due to the positive bias in not just percentage cloud cover (Kato et al. 2018), but the well-known systematic overestimation in MODIS-derived cloud droplet size (Painemal and Zuidema 2011). Larger particles lead to more forward scattering (Plass and Kattawar 1968), which could contribute to the positive bias in $K_{\downarrow,d}$ at the surface while simultaneously reducing $K_{\downarrow,b}$.

Although the relationships between annual cloud cover and annual $K_{\downarrow,b}$ (and $K_{\downarrow,d}$) for each gridded product are not consistently strong, we find the expected direction of sensitivity to cloud cover in all the datasets. The sensitivities are positive for $K_{\downarrow,d}$, ranging from 0.22 W m^{-2} per cloud cover percentage in MERRA-2 to 0.87 W m^{-2} per cloud cover percentage in NOAA–CIRES–DOE, and negative for $K_{\downarrow,b}$, ranging from −0.47 W m^{-2} per cloud cover percentage in MERRA-2 to −2.89 W m^{-2} per cloud cover percentage in NOAA–CIRES–DOE. Overall, the collinearity between cloud cover and $K_{\downarrow,b}$ is higher than for $K_{\downarrow,d}$. The individual scatterplots between $K_{\downarrow,d}$ (and $K_{\downarrow,b}$) and cloud cover percentage are also in Fig. S6 in the online supplemental material. Although there are large uncertainties in both cloud and aerosol representation in coarse-gridded models, that the interproduct variability of these atmospheric constituents controls the interproduct variability in the surface radiation fields is a reasonable assumption. This is because the top of the atmosphere incoming $K_{\downarrow}$ has strong theoretical constraints and varies between 340.3 W m^{-2} in NOAA–CIRES–DOE to 341.9 W m^{-2} in NCEP–NCAR for Common Period I. It is harder to separate the relative importance of the individual constituents due to the structural and parametric differences between these products. Cloud-radiation interactions depend

not only on aerial coverage of clouds, but also on cloud thickness and cloud optical properties, usually represented by the cloud optical depth (COD). For instance, an underestimation of cloud cover and an overestimation of COD can lead to a positive bias in $K_{\downarrow,b}$ and a negative bias in $K_{\downarrow,d}$ with minimal impact on overall $K_{\downarrow}$, which is seen in ERA5 (Table 2). In contrast, CERES, which has much higher cloud cover than ERA5 (Fig. 5), shows a negative bias in $K_{\downarrow,b}$ and a positive bias in $K_{\downarrow,d}$, which may be due to either the larger cloud droplet size or underestimated COD or a combination of both (Minnis et al. 2011). The overestimation of optically thick clouds in models relative to satellite observations has been known for a while (Zhang et al. 2005) but has not been used to specifically examine the differences in direct/diffuse partitioning among models. Although COD is not publicly archived in most of these reanalysis products, preventing such an analysis in the present study, accurately representing both overall cloud cover and COD might reduce this large variability in direct/diffuse partitioning across these products. The reanalysis products also have large differences in aerosol representation. The NOAA–CIRES–DOE and NCEP–NCAR reanalysis do not include tropospheric aerosols (although NOAA–CIRES–DOE has volcanic aerosols), ERA5 and JRA-55 consider aerosol climatology, and MERRA-2 includes time-varying assimilated aerosols and is the only one of these products that archives AOD. Thus, a similar analysis using all gridded products is not possible for the interproduct variability in aerosols.

We also examined the long-term trends in clouds and aerosols for Europe and China. Figures 6a–f show the correlation between the trends in cloud cover and the trends in $K_{\downarrow}$ and $K_{\downarrow,d}$ for Europe and China among the six datasets. Common Period I is used for CERES and Common Period II for the reanalysis products. For Europe in particular, these correlations are strong ($r^2 = 0.92$ for $K_{\downarrow,b}$ and 0.80 for $K_{\downarrow,d}$; Figs. 6c and 6e), suggesting that the strength of the brightening over these regions in the gridded data is primarily a function of the trends in the modeled cloud cover. All the datasets other than JRA-55 show a decrease in cloud cover over this region between 1980 and 2015 (Common Period II). We also calculate the trend in AOD for Europe from the MERRA-2 data (Fig. 6g), showing a decreasing trend of 0.04 per decade during the same period. The decrease in aerosol for Europe has been previously seen using both observations and models (Yang et al. 2020). Since aerosols generally increase $K_{\downarrow,d}$, keeping all other factors constant, this would explain the simultaneous decadal increase in $K_{\downarrow}$ and decrease in $K_{\downarrow,d}$ over Europe. For China, cloud cover decreases in most of the gridded products (other than JRA-55), with the magnitudes of change roughly half of that seen over Europe. The correlation between trends in cloud cover and trends in $K_{\downarrow}$ is relatively weak, though this is primarily driven by MERRA-2 being an outlier (r^2 increases to 0.88 if MERRA-2 is not used in this regression). Incidentally, only MERRA-2 assimilates observations of aerosols, showing an increase in AOD by 0.03 per decade over this region (Fig. 6h). Moreover, according to the grid-averaged trends, $K_{\downarrow,d}$ decreased during this period over China. This pattern could be due to the relative change in absorbing and scattering aerosols over the region during this time period. MERRA-2 data show a stronger increase in absorbed AOD relative to scattered AOD over China during Common Period II, suggesting a relative enhancement in absorbing aerosols (Fig. 6h). Even though the absorbing component of total AOD in MERRA-2 is modeled, not assimilated, observations bear out the increase in absorbing aerosols over China during this period (Schwarz et al. 2020).

Since in addition to cloud cover, MERRA-2 assimilates gridded AOD, we can estimate the sensitivity of the trends in $K_{\downarrow}$ and $K_{\downarrow,d}$ due to the trends in cloud cover and aerosols by solving this system of two equations:

$$\frac{K_{R,\mathrm{Tr,Eu}}}{K_{R,80,\mathrm{Eu}}} = a\frac{\mathrm{CLD}_{R,\mathrm{Tr,Eu}}}{\mathrm{CLD}_{R,80,\mathrm{Eu}}} + b\frac{\mathrm{AOD}_{R,\mathrm{Tr,Eu}}}{\mathrm{AOD}_{R,80,\mathrm{Eu}}} \quad \text{and} \tag{1}$$

$$\frac{K_{R,\mathrm{Tr,Ch}}}{K_{R,80,\mathrm{Ch}}} = a\frac{\mathrm{CLD}_{R,\mathrm{Tr,Ch}}}{\mathrm{CLD}_{R,80,\mathrm{Ch}}} + b\frac{\mathrm{AOD}_{R,\mathrm{Tr,Ch}}}{\mathrm{AOD}_{R,80,\mathrm{Ch}}}. \tag{2}$$

Here, subscripts "R,Tr,Eu" and "R,Tr,Ch" represent the trends in the MERRA-2 gridded products for Europe and China, respectively. The variables considered are the incoming radiation (K_R; either $K_{\downarrow}$ or $K_{\downarrow,d}$), the cloud cover (CLD), and AOD. Since these variables have different ranges, they are normalized by the value of the variable for the base year (1980; denoted by subscripts "R,80,Eu" and "R,80,Ch") to represent the fractional rates of change. For reference, $\mathrm{CLD}_{R,80,\mathrm{Eu}}$ and $\mathrm{CLD}_{R,80,\mathrm{Ch}}$ are 63.56% and 47.95%, respectively, whereas $\mathrm{AOD}_{R,80,\mathrm{Eu}}$ and $\mathrm{AOD}_{R,80,\mathrm{Ch}}$ are 0.26 and 0.18. Also, a and b are the unitless coefficients that give the sensitivity of the fraction rate of change in the radiation components to the fractional rate of change in CLD and AOD, respectively. Simultaneously solving these two equations, we find that both a and b are negative for fractional rate of change in $K_{\downarrow}$ ($a = -0.184$; $b = -0.037$) and positive for the corresponding fractional rate of change in $K_{\downarrow,d}$ ($a = 1.074$; $b = 0.124$). These values make sense physically since an increase in aerosols and clouds tends to decrease $K_{\downarrow}$ and increase $K_{\downarrow,d}$. In terms of magnitude, clouds play a stronger role than aerosols, with the sensitivity being almost 9 times as high for clouds for $K_{\downarrow,d}$ and 5 times as strong for $K_{\downarrow}$. Over Europe, the effect of clouds and aerosols reinforce each other, with both decreasing, thereby increasing $K_{\downarrow}$ and decreasing $K_{\downarrow,d}$. Over China, the total effect of aerosols, controlled by both the lower sensitivity to aerosols and the much higher fractional rate of change in AOD, overwhelm the impact of clouds, with $K_{\downarrow}$ decreasing despite a decrease in cloud cover.

We use this framework to constrain the sensitivity of $K_{\downarrow}$ and $K_{\downarrow,d}$ to CLD and AOD in the MERRA-2 dataset because of its conceptual simplicity. For comparison, we also used multilinear regressions to examine the trend in $K_{\downarrow}$ and $K_{\downarrow,d}$ as a function of grid-averaged CLD and AOD separately for Europe and China, given by the equation

$$\frac{K_R}{K_{R,80}} = \beta_0 + \beta_1\frac{\mathrm{CLD}_R}{\mathrm{CLD}_{R,80}}\beta_2\frac{\mathrm{AOD}_R}{\mathrm{AOD}_{R,80}}. \tag{3}$$

Here, the annual average values of $K_{\downarrow}$ and $K_{\downarrow,d}$ (K_R), CLD (CLD_R), and AOD (AOD_R) are normalized by their 1980

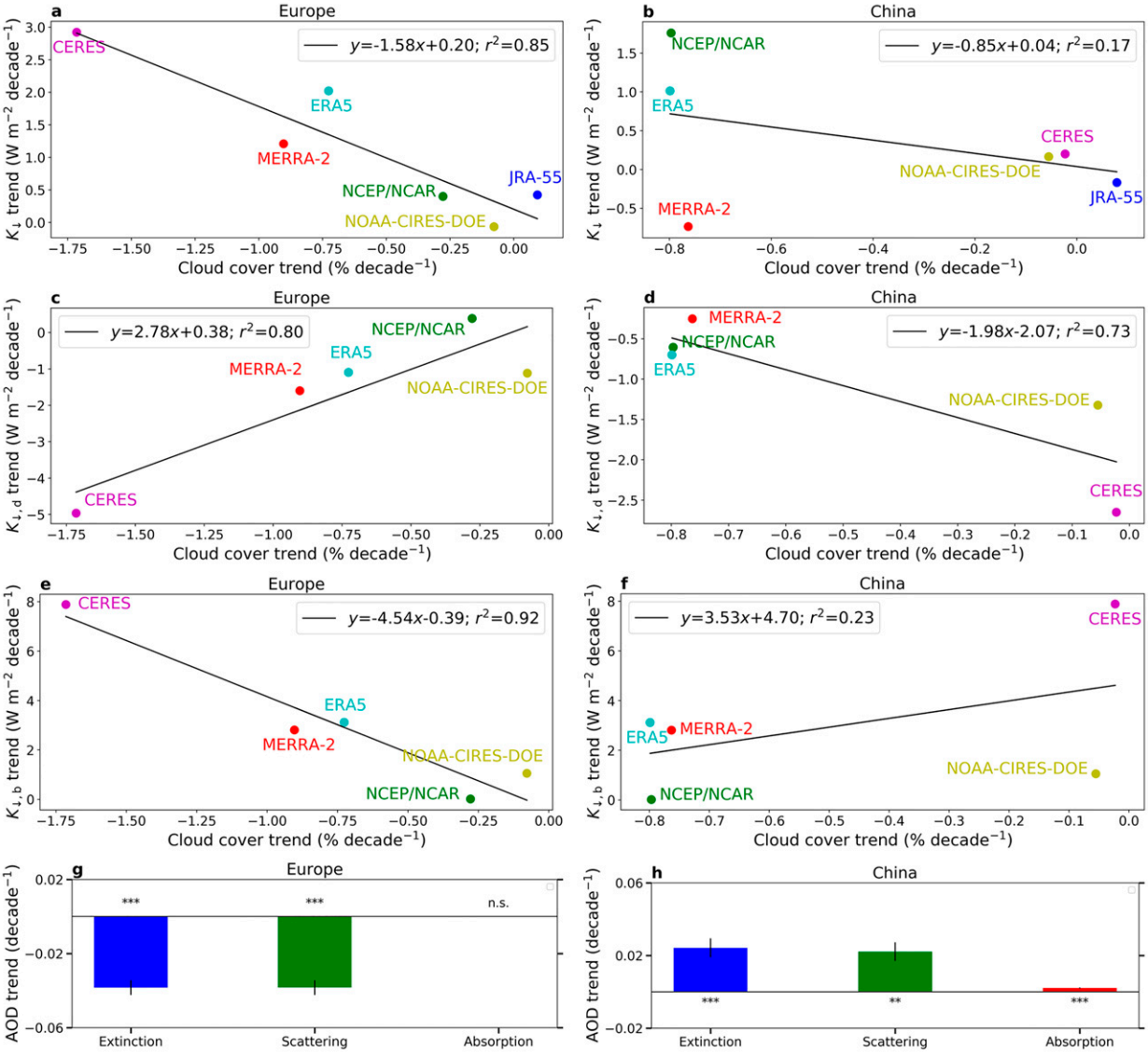

FIG. 6. Linear regressions between trends in grid-area-averaged percentage cloud cover and trends in (a),(b) $K_{\downarrow}$; (c),(d) $K_{\downarrow,d}$; and (e),(f) $K_{\downarrow,b}$ over (left) Europe and (right) China for all of the gridded products during Common Period II (1980–2015) for the reanalysis products and Common Period I (2001–15) for CERES. The equations for the lines of best fit are annotated. Also shown are trends in grid-area-averaged aerosol optical depth, separated into the scattering and absorbing components, for Common Period II as assimilated by MERRA-2 for (g) Europe and (h) China; the black lines show the standard errors, and the p values are indicated by asterisks, with three asterisks representing $p < 0.0001$, two for $p < 0.001$, and one for $p < 0.05$, with n.s. indicating no significance at the 0.05 level.

values and β_0, β_1, and β_2 are the coefficients of regression. Although the results are different over the two regions since they are not mathematically constrained by the same sensitivity as was done for Eqs. (1) and (2), we get the same signs and similar relative magnitudes of the regression coefficients. The terms β_1 and β_2 are always positive for $K_{\downarrow,d}$ and always negative for $K_{\downarrow}$. Clouds play a stronger role in both Europe and China for $K_{\downarrow}$ (β_1/β_2 = 14.52 and 6.26, respectively) and $K_{\downarrow,d}$ (β_1/β_2 = 3.57 and 8.03, respectively).

4. Discussion and summary

a. *Comparison with other modeled and satellite-derived estimates*

We are not aware of any formalized attempts to evaluate $K_{\downarrow,d}$ in current-generation CMIP6 models or their previous iterations. Although operational GCMs may sometimes lead reanalysis products in model development efforts (e.g., frequently using prognostic aerosols instead of prescribed aerosol distributions), many of the radiation codes and cloud

parameterizations used to generate the reanalysis products are also implemented in those models. Additionally, the fact that GCMs are run with fewer constraints on the atmospheric and surface variables than reanalysis products suggests that there may also be wide disparities in the $K_{\downarrow,d}$ modeled by GCMs. We see evidence of this from two studies that have evaluated $K_{\downarrow,d}$ at larger scales. Mercado et al. (2009) used radiative transfer calculations to simulate $K_{\downarrow,b}$ and $K_{\downarrow,d}$ globally. Using a subset of GEBA observations over Europe, Germany, and China, they evaluated their modeled $K_{\downarrow}$ and k_d. For GEBA stations in Germany and Europe, they found an underestimation in $K_{\downarrow}$ and an overestimation in k_d. Over China, their model overestimated $K_{\downarrow}$, but correctly simulated k_d, suggesting an overestimation in $K_{\downarrow,d}$. More recently, Chakraborty et al. (2021) used the latest version (version 6) of the Community Atmosphere Model (CAM6; Gettelman et al. 2019) to simulate $K_{\downarrow,d}$ and $K_{\downarrow,b}$ and evaluated the modeled values using all available GEBA observations. CAM6 overestimated $K_{\downarrow}$ and underestimated $K_{\downarrow,d}$, leading to an MBE of -0.08 for k_d for all GEBA sites.

Our evaluation of the CERES dataset shows that, while CERES does a great job at capturing both the magnitude and variability in $K_{\downarrow}$ (Table 2), there are issues with the direct/diffuse partitioning. CERES overestimates $K_{\downarrow,d}$ and underestimates $K_{\downarrow,b}$, leading to an overestimation in k_d (roughly 0.09 for all GEBA sites; Table 2), potentially caused by higher cloud fraction and cloud droplet size in satellite-derived products (Painemal and Zuidema 2011; Kato et al. 2018). In this context, a few other satellite-derived $K_{\downarrow,d}$ products also warrant discussion. Recently, Jiang et al. (2020) evaluated the $K_{\downarrow,d}$ in a recent dataset (JiEA) created using a deep learning algorithm and geostationary satellite measurements (Jiang et al. 2019a). Using 39 observation sites over East Asia, they found much better performance of the JiEA product when compared with ERA5. Consistent with our results, ERA5 underestimated $K_{\downarrow,d}$ (MBE $= -17.2\,\mathrm{W\,m^{-2}}$; $-1.2\,\mathrm{W\,m^{-2}}$ for JiEA) over their study area. The grid-area averaged k_d over East Asia was 0.42 for JiEA and 0.35 for ERA5. For China, which covers a large part of their study area, the grid-averaged k_d for the same time period (2007–14) varies from only 0.27 in the MERRA-2 dataset to roughly double that value (0.56) in the CERES data. Over Europe and Africa, the Copernicus Atmosphere Monitoring Service (CAMS) provides $K_{\downarrow}$, $K_{\downarrow,d}$, and $K_{\downarrow,b}$ estimates every 15 min based on the "Heliosat-4" method using Meteosat geostationary satellite observations (Qu et al. 2017). We estimated $K_{\downarrow,d}$ over the region of Europe (CAMS radiation service dataset "AGATE") covered by these satellites for Common Period I and found the regional average $K_{\downarrow,d}$ to range from $52.8\,\mathrm{W\,m^{-2}}$ in MERRA-2 to 102.6 in CERES versus a value of $65.4\,\mathrm{W\,m^{-2}}$ in CAMS. Another recent study produced global datasets of $K_{\downarrow}$, total photosynthetically active radiation (PAR) and its diffuse component from 2000 to 2016 by combining a radiative transfer model with an artificial neural network trained using MODIS data (Ryu et al. 2018). They calculated a global average ratio of 0.41 for diffuse PAR to total PAR and 0.46 for total PAR to $K_{\downarrow}$.

Of the data products we consider, only MERRA-2, NOAA–CIRES–DOE, and NCEP–NCAR publicly archive the diffuse portion of PAR. For Common Period I, we find large differences in these estimates for the three datasets for both diffuse PAR to total PAR (0.37 for MERRA-2; 0.54 for NOAA–CIRES–DOE; 0.46 for NCEP–NCAR) and for total PAR to $K_{\downarrow}$ (0.44 for MERRA-2; 0.52 for NOAA–CIRES–DOE; 0.61 for NCEP–NCAR). In comparison, the values of diffuse PAR to total PAR and of total PAR to $K_{\downarrow}$ in the CAM simulations by Chakraborty et al. (2021) were 0.41 and 0.51, respectively.

b. Limitations

Point observations have been frequently used to compare with gridded estimates of surface radiation (Markovic et al. 2009; Zhao et al. 2013; Wild et al. 2015). However, radiation transfer calculations in GCMs and reanalyses are based on the plane-parallel approximation, the assumption of one-dimensional atmospheric grids with horizontal planes as the upper and lower bounds, for computational efficiency. The real atmosphere has 3D cloud structures, particularly relevant for cloud–radiation interactions. For instance, cloud side illumination is the interception of radiation due to the existence of cloud sides in the real atmosphere, which are not captured by their plane-parallel approximations—a major issue at high solar zenith angles (Schäfer et al. 2016). Similarly, for low zenith angles, cloud side leakage causes more radiation to pass through the edges of clouds and reach the surface, which would be blocked in a plane-parallel representation (Ham et al. 2014). The overall result of these two mechanisms is generally an underestimation in simulated $K_{\downarrow}$ even when the cloud fraction is correctly captured by the approximation (Okata et al. 2017). Thus, these two effects on their own cannot explain the systematic overestimation in $K_{\downarrow}$ we find in the gridded products (Table 2). Cloud sky leakage would normally lead to more forward scattering and may thus increase $K_{\downarrow,d}$ in regions with low zenith angle, which we do find in the GEBA observations when compared with the MERRA-2 and ERA5 datasets. The effect of cloud side illumination, on the other hand, primarily blocks $K_{\downarrow,b}$ (Hogan and Shonk 2013), which would overestimate $K_{\downarrow,b}$ in GCMs, which is seen in all reanalysis products other than NOAA–CIRES–DOE (Table 2).

These problems are most serious at shorter time scales, as patchy clouds can cause large fluctuations in the observations at individual sites. Thus, since the signs of these 3D effects largely depend on zenith angle, the errors are reduced substantially when using monthly means since this averages over the various zenith angles (as was done here) and by combining the biases over multiple sites in a region. Note that the bias errors found here may also be related to other aspects of the 3D cloud structure, such as how overlap of clouds at various heights is represented (Wang et al. 2016). However, the intermodel variability is not affected by these issues since all the products considered use similar approximations. We find that this variability for both $K_{\downarrow,d}$ and $K_{\downarrow,b}$ is strongly controlled by cloud fraction (Fig. 4). Additional differences are also expected due to the shortwave parameterizations used in these datasets that convert the cloud representations to the radiances across wavelength channels. However, such an evaluation requires a modeling setup that controls for the

different inputs to the radiative transfer models used in the gridded products and hyperspectral observations for validation (Aumann et al. 2018).

A quantitative comparison of the long-term trends using observations requires consistent data coverage. The GEBA data are not always appropriate for this purpose because the trends in $K_{\downarrow,d}$ and $K_{\downarrow}$ (circles and hatched bars, Fig. 4) are derived from two different subsets of the data (there are more $K_{\downarrow}$ observations than $K_{\downarrow,d}$ observations). Moreover, even within Common Period II, the data coverage changes over time. This lack of consistent data coverage is particularly relevant for China since many studies find a reversal of the trends somewhere between 1990 and 2000, potentially influenced by the instrument changes after 1993 (Wang and Yang 2014). We try to account for potential breakpoints in the trends by testing for homogeneity of the time series. However, this reduces the number of available stations substantially, particularly over China (Fig. 4). As such, although the intermodel variability in long-term trends in the gridded datasets illustrates the differences between these models, we advise caution when talking about the "real" regional trends using GEBA observations, particularly for $K_{\downarrow,d}$ given the dearth of available observations. For China, one alternative is to use data from the China Meteorological Data Service Center (http://data.cma.cn). However, as seen in Wang et al. (2020), after testing for homogeneity, only 12 stations are available with long-term observations of both $K_{\downarrow}$ and $K_{\downarrow,d}$. An in-depth analysis of the influence of station and year range selection on these trends is in Schwarz et al. (2020), though they do not focus on $K_{\downarrow,d}$. Given that we find that the gridded data cannot generally capture either the direction or the variability in trends across the available GEBA sites for the corresponding time periods, further work is necessary to evaluate long-term trends in $K_{\downarrow,d}$ across CMIP6 models with consolidated observational databases that include both regional and global networks.

c. Summary

We find large differences in $K_{\downarrow,d}$, $K_{\downarrow,b}$, and k_d across current-generation gridded products. The variability is evident from the monthly to the annual scales and show large biases from observational benchmarks. For 2001–15, the range of variability is 10.7% for global mean $K_{\downarrow}$ (185.4–205.3 W m^{-2}), 60.4% for global mean $K_{\downarrow,b}$ (82.8–132.8 W m^{-2}), 94.3% for global mean $K_{\downarrow,d}$ (52.8–102.6 W m^{-2}), and 96.4% for global mean k_d (0.28–0.55). The variability between these products is statistically explained by the biases in modeled cloud fraction. Long-term (1980–2015) trends in the two variables also differ over Europe and China and are not captured well by the gridded products. These intermodel differences in $K_{\downarrow,d}$ would affect Earth system simulations, particularly relevant for surface climate and for estimating solar energy potential. Thus, we suggest comprehensive comparisons of simulated k_d in the CMIP6 models to better identify potential deficiencies in current-generation atmosphere models.

Acknowledgments. We acknowledge the Computational and Information Systems Laboratory at the National Center for Atmospheric Research (NCAR), the Yale Center for Earth Observation (YCEO), and Microsoft (through an AI for Earth grant) for providing computational resources. This research is supported in part by the U.S. National Science Foundation (Grant AGS1933630).

Data availability statement. The CERES data were obtained from the NASA Langley Research Center CERES ordering tool (https://ceres.larc.nasa.gov/). The NOAA–CIRES–DOE and NCEP–NCAR reanalysis datasets were downloaded from the PSL website (https://psl.noaa.gov/). The MERRA-2 reanalysis dataset can be found on NASA's website (https://gmao.gsfc.nasa.gov/reanalysis/MERRA-2/). The ERA5 reanalysis data were downloaded from the Copernicus Climate Data Store (https://cds.climate.copernicus.eu/). The JRA-55 reanalysis data were downloaded from NCAR's Research Data Archive (https://rda.ucar.edu/). The CAMS dataset for Europe was obtained online (http://www.soda-pro.com/).

REFERENCES

Alexandersson, H., 1986: A homogeneity test applied to precipitation data. *J. Climatol.*, **6**, 661–675, https://doi.org/10.1002/joc.3370060607.

Aumann, H. H., and Coauthors, 2018: Evaluation of radiative transfer models with clouds. *J. Geophys. Res.*, **123**, 6142–6157, https://doi.org/10.1029/2017JD028063.

Bosilovich, M. G., F. R. Robertson, and J. Chen, 2011: Global energy and water budgets in MERRA. *J. Climate*, **24**, 5721–5739, https://doi.org/10.1175/2011JCLI4175.1.

Briegleb, B. P., 1992: Delta-Eddington approximation for solar radiation in the NCAR Community Climate Model. *J. Geophys. Res.*, **97**, 7603–7612, https://doi.org/10.1029/92JD00291.

Buchard, V., and Coauthors, 2017: The MERRA-2 aerosol reanalysis, 1980 onward. Part II: Evaluation and case studies. *J. Climate*, **30**, 6851–6872, https://doi.org/10.1175/JCLI-D-16-0613.1.

Chakraborty, T., and X. Lee, 2019: Land cover regulates the spatial variability of temperature response to the direct radiative effect of aerosols. *Geophys. Res. Lett.*, **46**, 8995–9003, https://doi.org/10.1029/2019GL083812.

——, ——, and D. Lawrence, 2021: Strong local evaporative cooling over land due to atmospheric aerosols. *J. Adv. Model. Earth Syst.*, **13**, e2021MS002491, https://doi.org/10.1029/2021MS002491.

Chou, M.-D., and M. J. Suarez, 1999: A solar radiation parameterization for atmospheric studies. NASA Tech. Memo. NASA/TM-1999-104606, Vol. 15, 38 pp., https://ntrs.nasa.gov/api/citations/19990060930/downloads/19990060930.pdf.

Feng, Y., D. Chen, and X. Zhao, 2018: Estimated long-term variability of direct and diffuse solar radiation in North China during 1959–2016. *Theor. Appl. Climatol.*, **137**, 153–163, https://doi.org/10.1007/s00704-018-2579-1.

Freidenreich, S., and V. Ramaswamy, 1999: A new multiple-band solar radiative parameterization for general circulation models. *J. Geophys. Res.*, **104**, 31 389–31 409, https://doi.org/10.1029/1999JD900456.

Gettelman, A., and Coauthors, 2019: The Whole Atmosphere Community Climate Model version 6 (WACCM6). *J. Geophys. Res.*, **124**, 12 380–12 403, https://doi.org/10.1029/2019JD030943.

Gilgen, H., and A. Ohmura, 1999: The Global Energy Balance Archive. *Bull. Amer. Meteor. Soc.*, **80**, 831–850, https://doi.org/10.1175/1520-0477(1999)080<0831:TGEBA>2.0.CO;2.

Ham, S. H., S. Kato, H. W. Barker, F. G. Rose, and S. Sun-Mack, 2014: Effects of 3-D clouds on atmospheric transmission of solar radiation: Cloud type dependencies inferred from A-Train satellite data. *J. Geophys. Res.*, **119**, 943–963, https://doi.org/10.1002/2013JD020683.

Hersbach, H., and Coauthors, 2020: The ERA5 global reanalysis. *Quart. J. Roy. Meteor. Soc.*, **146**, 1999–2049, https://doi.org/10.1002/qj.3803.

Hogan, R. J., and J. K. Shonk, 2013: Incorporating the effects of 3D radiative transfer in the presence of clouds into two-stream multilayer radiation schemes. *J. Atmos. Sci.*, **70**, 708–724, https://doi.org/10.1175/JAS-D-12-041.1.

Hou, Y.-T., S. Moorthi, and K. Campana, 2002: Parameterization of solar radiation transfer in the NCEP models. NCEP Office Note 441, 46 pp., https://repository.library.noaa.gov/view/noaa/23085.

Jiang, H., N. Lu, J. Qin, W. Tang, and L. Yao, 2019a: A deep learning algorithm to estimate hourly global solar radiation from geostationary satellite data. *Renew. Sustain. Energy Rev.*, **114**, 109327, https://doi.org/10.1016/j.rser.2019.109327.

——, Y. Yang, Y. Bai, and H. Wang, 2019b: Evaluation of the total, direct, and diffuse solar radiations from the ERA5 reanalysis data in China. *IEEE Geosci. Remote Sens. Lett.*, **17**, 47–51, https://doi.org/10.1109/LGRS.2019.2916410.

——, ——, H. Wang, Y. Bai, and Y. Bai, 2020: Surface diffuse solar radiation determined by reanalysis and satellite over East Asia: Evaluation and comparison. *Remote Sens.*, **12**, 1387, https://doi.org/10.3390/rs12091387.

Kalnay, E., and Coauthors, 1996: The NCEP/NCAR 40-Year Reanalysis Project. *Bull. Amer. Meteor. Soc.*, **77**, 437–472, https://doi.org/10.1175/1520-0477(1996)077<0437:TNYRP>2.0.CO;2.

Kato, S., and Coauthors, 2018: Surface irradiances of edition 4.0 Clouds and the Earth's Radiant Energy System (CERES) energy balanced and filled (EBAF) data product. *J. Climate*, **31**, 4501–4527, https://doi.org/10.1175/JCLI-D-17-0523.1.

Kennedy, A. D., X. Dong, B. Xi, S. Xie, Y. Zhang, and J. Chen, 2011: A comparison of MERRA and NARR reanalyses with the DOE ARM SGP data. *J. Climate*, **24**, 4541–4557, https://doi.org/10.1175/2011JCLI3978.1.

Kistler, R., and Coauthors, 2001: The NCEP–NCAR 50-Year Reanalysis: Monthly means CD-ROM and documentation. *Bull. Amer. Meteor. Soc.*, **82**, 247–268, https://doi.org/10.1175/1520-0477(2001)082<0247:TNNYRM>2.3.CO;2.

Knohl, A., and D. D. Baldocchi, 2008: Effects of diffuse radiation on canopy gas exchange processes in a forest ecosystem. *J. Geophys. Res. Biogeosci.*, **113**, G02023, https://doi.org/10.1029/2007JG000663.

Kobayashi, S., and Coauthors, 2015: The JRA-55 reanalysis: General specifications and basic characteristics. *J. Meteor. Soc. Japan*, **93**, 5–48, https://doi.org/10.2151/jmsj.2015-001.

Lacis, A. A., and J. Hansen, 1974: A parameterization for the absorption of solar radiation in the Earth's atmosphere. *J. Atmos. Sci.*, **31**, 118–133, https://doi.org/10.1175/1520-0469(1974)031<0118:APFTAO>2.0.CO;2.

Lee, K.-T., and Coauthors, 2016: Concentrator photovoltaic module architectures with capabilities for capture and conversion of full global solar radiation. *Proc. Natl. Acad. Sci. USA*, **113**, E8210–E8218, https://doi.org/10.1073/pnas.1617391113.

Liu, B. Y., and R. C. Jordan, 1960: The interrelationship and characteristic distribution of direct, diffuse and total solar radiation. *Sol. Energy*, **4** (3), 1–19, https://doi.org/10.1016/0038-092X(60)90062-1.

Loeb, N. G., and Coauthors, 2019: Decomposing shortwave top-of-atmosphere and surface radiative flux variations in terms of surface and atmospheric contributions. *J. Climate*, **32**, 5003–5019, https://doi.org/10.1175/JCLI-D-18-0826.1.

Markovic, M., C. G. Jones, K. Winger, and D. Paquin, 2009: The surface radiation budget over North America: Gridded data assessment and evaluation of regional climate models. *Int. J. Climatol.*, **29**, 2226–2240.

Mercado, L. M., N. Bellouin, S. Sitch, O. Boucher, C. Huntingford, M. Wild, and P. M. Cox, 2009: Impact of changes in diffuse radiation on the global land carbon sink. *Nature*, **458**, 1014–1017, https://doi.org/10.1038/nature07949.

Minnis, P., and Coauthors, 2011: CERES edition-2 cloud property retrievals using TRMM VIRS and Terra and Aqua MODIS data—Part II: Examples of average results and comparisons with other data. *IEEE Trans. Geosci. Remote Sens.*, **49**, 4401–4430, https://doi.org/10.1109/TGRS.2011.2144602.

Morcrette, J., H. W. Barker, J. Cole, M. J. Iacono, and R. Pincus, 2008: Impact of a new radiation package, MCRAD, in the ECMWF Integrated Forecasting System. *Mon. Wea. Rev.*, **136**, 4773–4798, https://doi.org/10.1175/2008MWR2363.1.

Moseid, K. O., and Coauthors, 2020: Bias in CMIP6 models compared to observed regional dimming and brightening trends (1961–2014). *Atmos. Chem. Phys. Discuss.*, **20**, 16 023–16 040, https://doi.org/10.5194/acp-20-16023-2020.

Okata, M., T. Nakajima, K. Suzuki, T. Inoue, T. Y. Nakajima, and H. Okamoto, 2017: A study on radiative transfer effects in 3-D cloudy atmosphere using satellite data. *J. Geophys. Res.*, **122**, 443–468, https://doi.org/10.1002/2016JD025441.

Oreopoulos, L., and Coauthors, 2012: The continual intercomparison of radiation codes: Results from phase I. *J. Geophys. Res.*, **117**, 6118, https://doi.org/10.1029/2011JD016821.

Painemal, D., and P. Zuidema, 2011: Assessment of MODIS cloud effective radius and optical thickness retrievals over the southeast Pacific with VOCALS-REx in situ measurements. *J. Geophys. Res.*, **116**, 24206, https://doi.org/10.1029/2011JD016155.

Pfeifroth, U., A. Sanchez-Lorenzo, V. Manara, J. Trentmann, and R. Hollmann, 2018: Trends and variability of surface solar radiation in Europe based on surface- and satellite-based data records. *J. Geophys. Res.*, **123**, 1735–1754, https://doi.org/10.1002/2017JD027418.

Pincus, R., P. M. Forster, and B. Stevens, 2016: The Radiative Forcing Model Intercomparison Project (RFMIP): Experimental protocol for CMIP6. *Geosci. Model Dev.*, **9**, 3447–3460, https://doi.org/10.5194/gmd-9-3447-2016.

Plass, G. N., and G. W. Kattawar, 1968: Monte Carlo calculations of light scattering from clouds. *Appl. Opt.*, **7**, 415–419, https://doi.org/10.1364/AO.7.000415.

Qu, Z., A. Oumbe, and Coauthors, 2017: Fast radiative transfer parameterisation for assessing the surface solar irradiance: The Heliosat-4 method. *Meteor. Z.*, **26**, 33–57, https://doi.org/10.1127/metz/2016/0781.

Randles, C., and Coauthors, 2017: The MERRA-2 aerosol reanalysis, 1980 onward. Part I: System description and data assimilation evaluation. *J. Climate*, **30**, 6823–6850, https://doi.org/10.1175/JCLI-D-16-0609.1.

Rap, A., and Coauthors, 2018: Enhanced global primary production by biogenic aerosol via diffuse radiation fertilization. *Nat. Geosci.*, **11**, 640–644, https://doi.org/10.1038/s41561-018-0208-3.

Rutan, D. A., S. Kato, D. R. Doelling, F. G. Rose, L. T. Nguyen, T. E. Caldwell, and N. G. Loeb, 2015: CERES synoptic product: Methodology and validation of surface radiant flux. *J. Atmos. Oceanic Technol.*, **32**, 1121–1143, https://doi.org/10.1175/JTECH-D-14-00165.1.

Ryu, Y., C. Jiang, H. Kobayashi, and M. Detto, 2018: MODIS-derived global land products of shortwave radiation and diffuse and total photosynthetically active radiation at 5 km resolution from 2000. *Remote Sens. Environ.*, **204**, 812–825, https://doi.org/10.1016/j.rse.2017.09.021.

Saha, S., and Coauthors, 2010: The NCEP Climate Forecast System Reanalysis. *Bull. Amer. Meteor. Soc.*, **91**, 1015–1058, https://doi.org/10.1175/2010BAMS3001.1.

Samukova, E. A., E. V. Gorbarenko, and A. E. Erokhina, 2014: Long-term variations of solar radiation in Europe. *Russ. Meteor. Hydrol.*, **39**, 514–520, https://doi.org/10.3103/S1068373914080020.

Sanchez-Lorenzo, A., and Coauthors, 2015: Reassessment and update of long-term trends in downward surface shortwave radiation over Europe (1939–2012). *J. Geophys. Res.*, **120**, 9555–9569, https://doi.org/10.1002/2015JD023321.

Schäfer, S. A., R. J. Hogan, C. Klinger, J. C. Chiu, and B. Mayer, 2016: Representing 3-D cloud radiation effects in two-stream schemes: 1. Longwave considerations and effective cloud edge length. *J. Geophys. Res.*, **121**, 8567–8582, https://doi.org/10.1002/2016JD024876.

Schwarz, M., D. Folini, S. Yang, R. P. Allan, and M. Wild, 2020: Changes in atmospheric shortwave absorption as important driver of dimming and brightening. *Nat. Geosci.*, **13**, 110–115, https://doi.org/10.1038/s41561-019-0528-y.

Slivinski, L. C., and Coauthors, 2019: Towards a more reliable historical reanalysis: Improvements for version 3 of the Twentieth Century Reanalysis System. *Quart. J. Roy. Meteor. Soc.*, **145**, 2876–2908, https://doi.org/10.1002/qj.3598.

Stephens, G. L., and Coauthors, 2012: An update on Earth's energy balance in light of the latest global observations. *Nat. Geosci.*, **5**, 691–696, https://doi.org/10.1038/ngeo1580.

Wang, X., Y. Liu, and Q. Bao, 2016: Impacts of cloud overlap assumptions on radiative budgets and heating fields in convective regions. *Atmos. Res.*, **167**, 89–99, https://doi.org/10.1016/j.atmosres.2015.07.017.

Wang, Y. W., and Y. H. Yang, 2014: China's dimming and brightening: Evidence, causes and hydrological implications. *Ann. Geophys.*, **32**, 41–55, https://doi.org/10.5194/angeo-32-41-2014.

——, S. Yang, A. Sanchez-Lorenzo, W. Yuan, and M. Wild, 2020: A revisit of direct and diffuse solar radiation in China based on homogeneous surface observations: Climatology, trends, and their probable causes. *J. Geophys. Res.*, **125**, e2020JD032634, https://doi.org/10.1029/2020JD032634.

Wild, M., 2012: Enlightening global dimming and brightening. *Bull. Amer. Meteor. Soc.*, **93**, 27–37, https://doi.org/10.1175/BAMS-D-11-00074.1.

——, 2016: Decadal changes in radiative fluxes at land and ocean surfaces and their relevance for global warming. *Wiley Interdiscip. Rev.: Climate Change*, **7**, 91–107, https://doi.org/10.1002/wcc.372.

——, A. Ohmura, H. Gilgen, and J.-J. Morcrette, 1998: The distribution of solar energy at the Earth's surface as calculated in the ECMWF re-analysis. *Geophys. Res. Lett.*, **25**, 4373–4376, https://doi.org/10.1029/1998GL900175.

——, and Coauthors, 2015: The energy balance over land and oceans: An assessment based on direct observations and CMIP5 climate models. *Climate Dyn.*, **44**, 3393–3429, https://doi.org/10.1007/s00382-014-2430-z.

——, A. Ohmura, C. Schär, G. Müller, D. Folini, M. Schwarz, and M. Z. Hakuba, 2017: The Global Energy Balance Archive (GEBA) version 2017: A database for worldwide measured surface energy fluxes. *Earth Syst. Sci. Data*, **9**, 601–613, https://doi.org/10.5194/essd-9-601-2017.

Yang, S., X. L. Wang, and M. Wild, 2019: Causes of dimming and brightening in China inferred from homogenized daily clear-sky and all-sky in situ surface solar radiation records (1958–2016). *J. Climate*, **32**, 5901–5913, https://doi.org/10.1175/JCLI-D-18-0666.1.

Yang, Y., S. Lou, H. Wang, P. Wang, and H. Liao, 2020: Trends and source apportionment of aerosols in Europe during 1980–2018. *Atmos. Chem. Phys.*, **20**, 2579–2590, https://doi.org/10.5194/acp-20-2579-2020.

Yue, X., and N. Unger, 2017: Aerosol optical depth thresholds as a tool to assess diffuse radiation fertilization of the land carbon uptake in China. *Atmos. Chem. Phys.*, **17**, 1329–1342, https://doi.org/10.5194/acp-17-1329-2017.

Zhang, M. H., and Coauthors, 2005: Comparing clouds and their seasonal variations in 10 atmospheric general circulation models with satellite measurements. *J. Geophys. Res.*, **110**, D15S02, https://doi.org/10.1029/2004JD005021.

Zhang, X., S. Liang, G. Wang, Y. Yao, B. Jiang, and J. Cheng, 2016: Evaluation of the reanalysis surface incident shortwave radiation products from NCEP, ECMWF, GSFC, and JMA using satellite and surface observations. *Remote Sens.*, **8**, 225, https://doi.org/10.3390/rs8030225.

Zhao, L., X. Lee, and S. Liu, 2013: Correcting surface solar radiation of two data assimilation systems against FLUXNET observations in North America. *J. Geophys. Res.*, **118**, 9552–9564, https://doi.org/10.1002/jgrd.50697.

Copyright of Journal of Climate is the property of American Meteorological Society and its content may not be copied or emailed to multiple sites or posted to a listserv without the copyright holder's express written permission. However, users may print, download, or email articles for individual use.